Supporting Information

Experimental Activity Descriptors for Iridium-based Catalysts for the Electrochemical Oxygen Evolution Reaction (OER)

Camillo Spöri[a], Pascal Briois[b], Hong Nhan Nong[a,c], Tobias Reier[a], Alain Billard[b], Stefanie Kühl[a], Detre Teschner[c,d], and Peter Strasser[a,]*

a) The Electrochemical Catalysis, Energy and Materials Science Laboratory, Department of Chemistry, Technische Universität Berlin, Straße des 17. Juni 124, 10623 Berlin, Germany

b) FEMTO-ST (UMR CNRS 6174), Université de Bourgogne Franche-Comté, UTBM, 90010 Belfort, France

c) Max Planck Institute for Chemical Energy Conversion, Stiftstr. 34-36, 45470 Mülheim an der Ruhr, Germany

d) Fritz-Haber-Institut der Max-Planck Gesellschaft, Faradayweg 4–6, 14195 Berlin, Germany

AUTHOR INFORMATION

Corresponding Author

*Peter Strasser, pstrasser@tu-berlin.de

Initial electrochemical activities

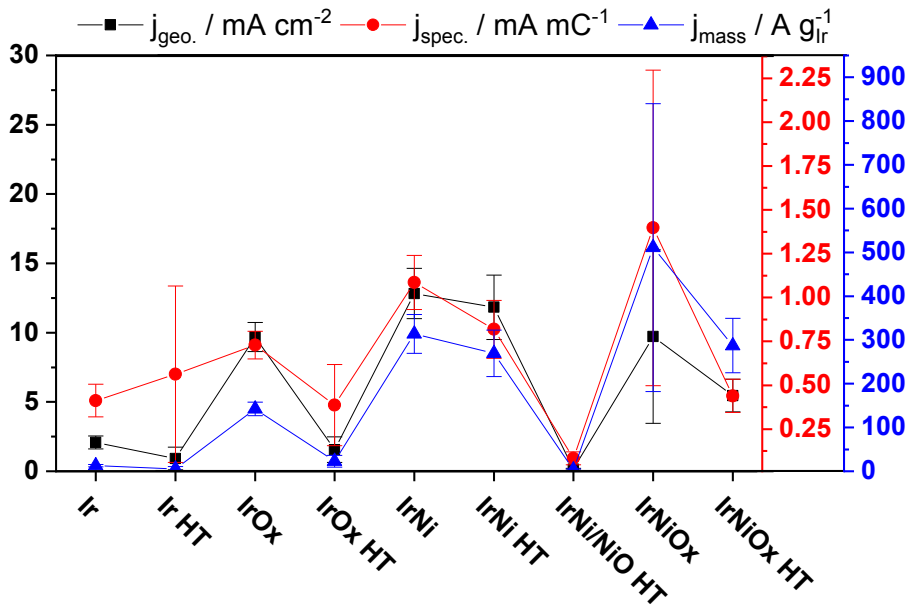

Fig. S1: Initial activities (geometric, specific and mass based) of all samples investigated at 1.53 V_{RHE} (300 mV overpotential, iR corrected), highlighting the detrimental effect of heat treatment on the activity.

Fig. S1 illustrates the detrimental influence of heat-treating on the initial activity (taken from the SPV measured at the beginning of the electrochemical protocol – see experimental section below) before further effects such as catalyst loss can set in. Initially, all non-heat-treated samples except *IrNi HT* are more active than their heat-treated counterparts. However, caution has to be applied when interpreting this data as the initial scans can be superimposed with additional oxidation and dissolution currents, which is also represented by the larger error bars. Further initial activity data is given in Table S1.

Table S1: Initial activities as current densities at 1.53 V_{RHE} (iR corrected) taken from the first SPV technique (see electrochemical protocol)

sample	Initial activities		
	j_{geo} / mA cm^{-2}	j_{mass} / A g$^{-1}_{Ir}$	j_{spec} / mA cm^{-2}
	1.53 V		
Ir	2.1	13	0.41
Ir HT	0.9	6	0.56
IrNi	12.8	314	1.09
IrNi HT	11.8	269	0.82
IrNi/NiO HT	0.2	4	0.08
IrOx	9.7	142	0.73
IrOx HT	1.6	23	0.39
IrNiOx	9.7	511	1.40
IrNiOx HT	5.46	287	0.44

GI-XRD measurements

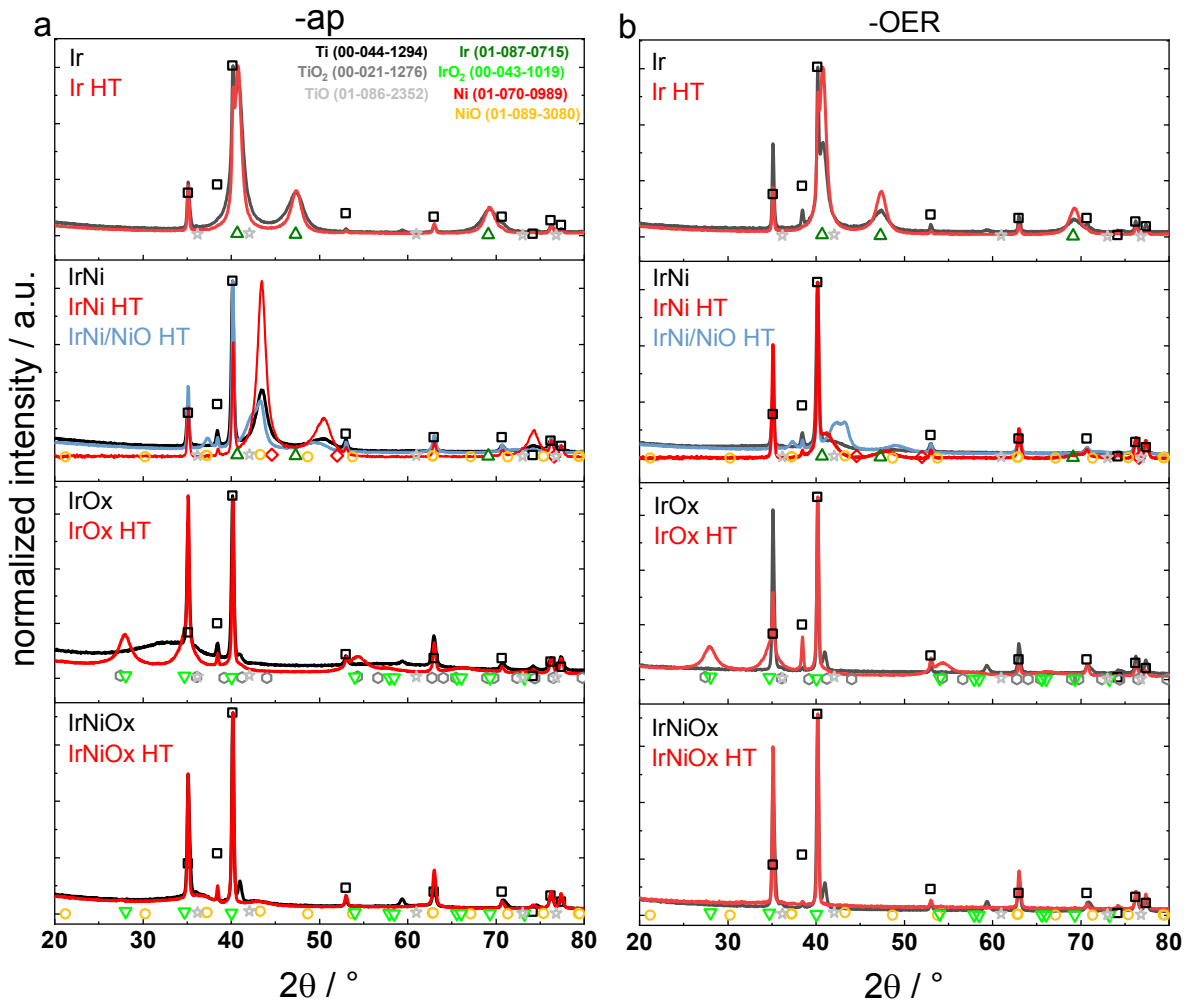

Fig. S2: XRD patterns of a) as prepared samples and b) samples after OER normalized to the highest intensity. Black and red curves depicting non- and heat-treated samples, respectively. Patterns of IrNi/NiO HT are depicted in light blue. Reference patterns from the PDF of possible phases are given as scatter plots below the data and indicated with the corresponding phase and index in the top right corner of the Ir-ap plot. The Ti substrate PDF is given as scatter plot with the corresponding normalized intensities for clarity.

Fig. S2 depicts the grazing-incidence XRD patterns recorded for all samples in their *–ap* (Fig. S2a) and *-OER* (Fig. S2b) states. Following Fig. S2A from top to bottom: The diffraction patterns for *Ir (HT)-ap* closely resemble those presented in literature with a slight increase in crystallinity after heat treatment.[1] On the IrNi alloy samples the IrNi (111) reflex position can be used for analysis of the alloy composition according to Vegard's law.[2] *IrNi (HT)-ap* show one distinct IrNi phase, fitting well to the alloy composition measured with SEM-EDX and XPS (83 at% Ni, see main manuscript). Heat treatment leads to a sharp increase in crystallinity for *IrNi HT-ap*. On *IrNi/NiO HT-ap* the heat treatment produces an additional phase that can be identified as NiO (bunsenite) by comparison to reference patterns from the PDF and Rietveld

refinement (see Fig. S3). Using Vegard's law reveals drastic changes in the composition of the remaining IrNi phase in *IrNi/NiO HT-ap* vs. *IrNi-ap* ($Ir_{70}Ni_{30}$ vs. $Ir_{17}Ni_{83}$) indicating the formation of a thick NiO layer.

The *IrOx HT-ap* diffraction pattern is well in line with the IrO_2 patterns of similarly calcined thin films presented elsewhere,[3-4] whereas the non-heat-treated *IrOx-ap* reveals a single, broad reflection around 34 °2θ only. *IrNiOx-ap* and *IrNiOx HT-ap* are completely x-ray amorphous, comparable to the template *IrNiOx TF* catalyst of similar composition[4]. Additionally, a small Ti-suboxide phase (TiO, Hongquiite) present on all non-heat-treated samples disappeared after thermal treatment (see Fig. S4).

After OER (Fig. S2b) the non-heat-treated samples show decreasing (metallic samples) to no (oxidic samples) XRD reflexes owing to observed catalyst loss (see Fig. S6 and SEM results in the main manuscript). Effectively, only *Ir-OER* and *IrNi (HT)-OER* can be attributed to the original phases with the IrNi reflexes shifting in relation to the Ni leaching observed in SEM-EDX. XRD patterns of *Ir HT-OER* and *IrOx HT-OER* remain unchanged to the -ap state. The *IrNi/NiO HT-OER* reflexes shift corresponding to *IrNi-OER,* but the observed NiO phase remains.

Rietveld refinement

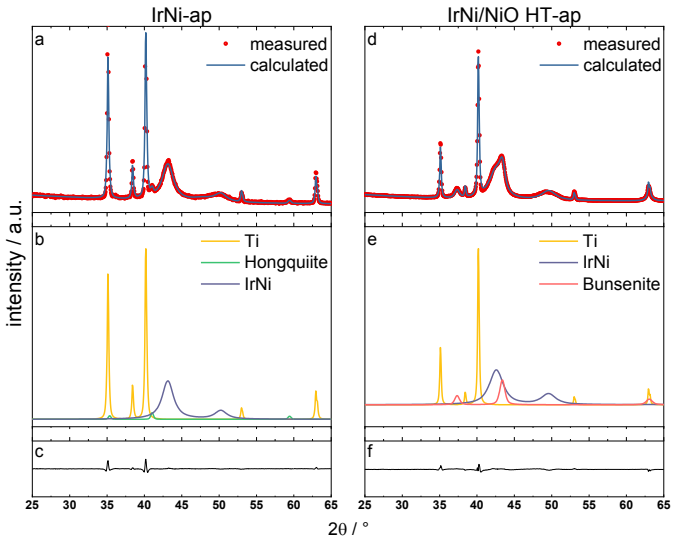

Fig. S3: Rietveld refinement of (left, a-c) IrNi-ap and (right, d-f) IrNi/NiO HT-ap. a) and d) measured and sum of the calculated profile, b) and e) single phase contributions and c) and f) difference between measured and calculated curves.

Fig. S3 depicts the Rietveld refinement of *IrNi-ap* and *IrNi/NiO HT-ap* to further elaborate on the appearance of the bunsenite NiO phase after heat treatment. On *IrNi-ap* the only additional phase is a TiOx suboxide (Hongquiite) phase, which disappears after heat treatment (see Fig. S4 below). The changes in the main reflex of the diffraction pattern for *IrNi/NiO HT-ap* allow multiple interpretations. Splitting of the (111) reflex

could be assigned to a phase separation into two IrNi phases of different composition or the emergence of an additional Ir phase, which could be possible due to the observed phase segregation during NiO formation (see discussion in the main text). The formation of IrO_2 or TiO_2 phases would fit the pattern change in the 40-55 °2θ range as well. However, the only single phase that can also explain the reflex around 37 °2θ is a pure NiO bunsenite phase. Using IrNi with a larger Ir content of ~70 % and NiO, the recorded patterns fit well. This is in line with further observations presented in the main text. Furthermore, the segregation and thickness of the formed NiO layer (following from the remaining IrNi composition of 70:30 in the IrNi layer) explains the missing Ir4f signal in the XPS analysis of *IrNi/NiO HT-ap*.

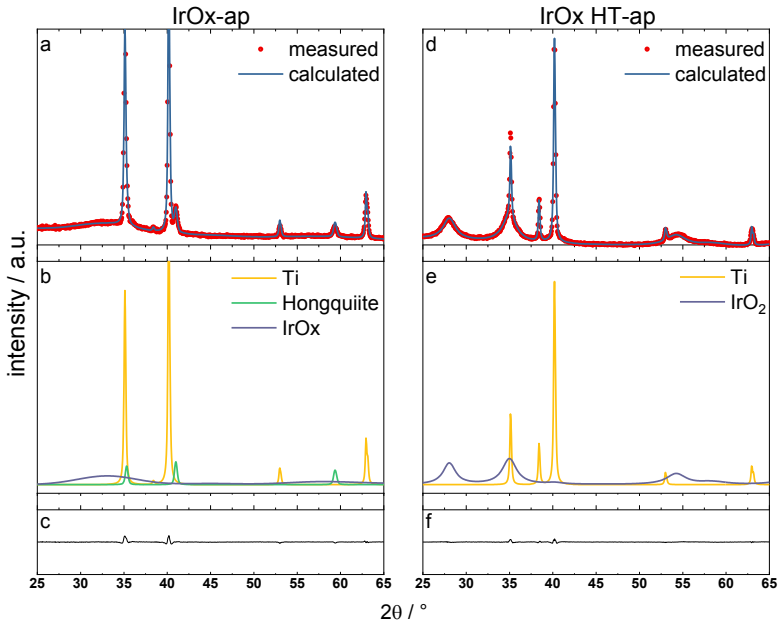

Fig. S4: Rietveld refinement of IrOx-ap (left, a-c) and IrOx HT-ap (right, d-f), exemplarily showing the existence of a hongquiite substoichiometric TiOx phase and its disappearance after heat treatment. a) and d) measured and sum of the calculated profile, b) and e) single phase contributions and c) and f) difference between measured and calculated curves.

Rietveld refinement of all –*ap* samples confirms the existence of a substoichoimetric hongquiite TiOx phase, as shown exemplarily for *IrOx-ap* in Fig. S4. The observed TiOx phase disappears after heat treatment on all samples independently of the heat treatment atmosphere. This suboxide phase most likely stems from transport of the substrates in air in between polishing and sputtering or from the acid leaching step applied after polishing.

SEM images

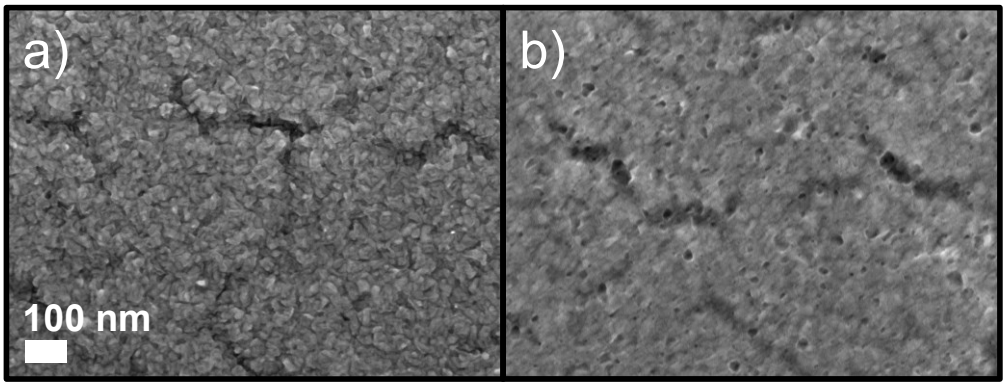

Fig. S5: SEM top view images of IrNi/NiO HT in the a) -ap and b) -OER state. Nanocrystalline platelets that formed on top of the IrNi surface are clearly visible after heat treatment. After OER testing the platelets have formed a condensed surface layer that exhibits various nanometer-sized holes.

Catalyst layer delamination after OER

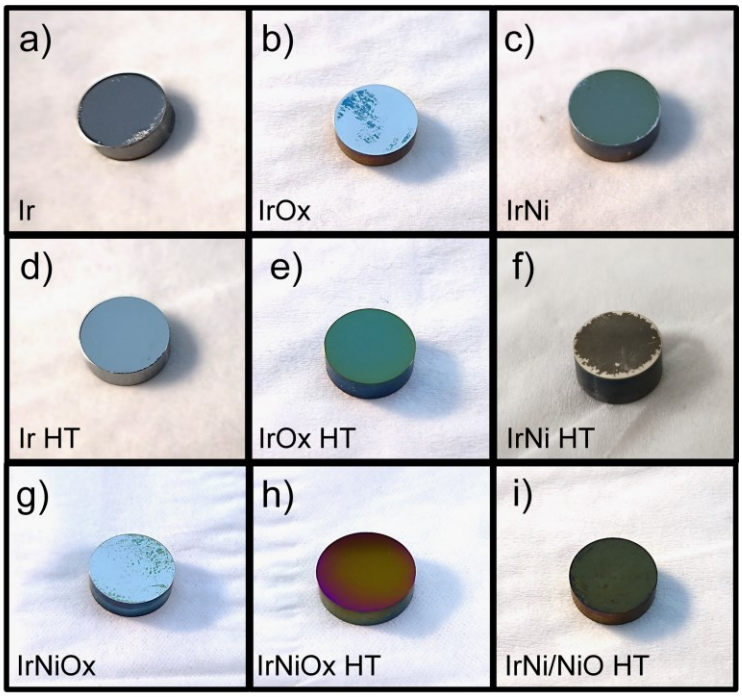

Fig. S6: Photos of the investigated catalysts in their -OER states. a) Ir, b) IrOx, c) IrNi, d) Ir HT, e) IrOx HT, f) IrNi HT, g) IrNiOx, h) IrNiOx HT, i) IrNi/NiO HT.

Fig. S6 reveals visible catalyst loss on the non-heat-treated catalysts after OER. Delamination is only visible to a small extent and confined to the edges on the metallic samples *Ir-OER* and *IrNi (HT)-OER* (Fig. S6a, c and f, respectively) whereas severe delamination almost to the extent of total catalyst loss is observed on the oxides *IrOx-OER* and *IrNiOx-OER* (Fig. S6b and g, respectively). On most of the heat-treated counterparts (Fig. S6d, e, h and i) no catalyst loss is observed visually and by SEM. Where catalyst layer

is lost, the Ti support could be easily oxidized to TiO_X species during the OER. For future studies, protective coatings such as Au or TiN could present a good mitigation strategy if the catalyst adhesion of a specific catalyst cannot be optimized.

Cross-section analysis

To elucidate the structure of the emerging NiO layer and its stability, (scanning) transmission electron microscopy (S/TEM), selected area electron diffraction (SAED), as well as STEM-EDX line scans were performed on a cross-section sample of *IrNi/NiO HT-OER*, which are described in the following (see Fig. S7-S11).

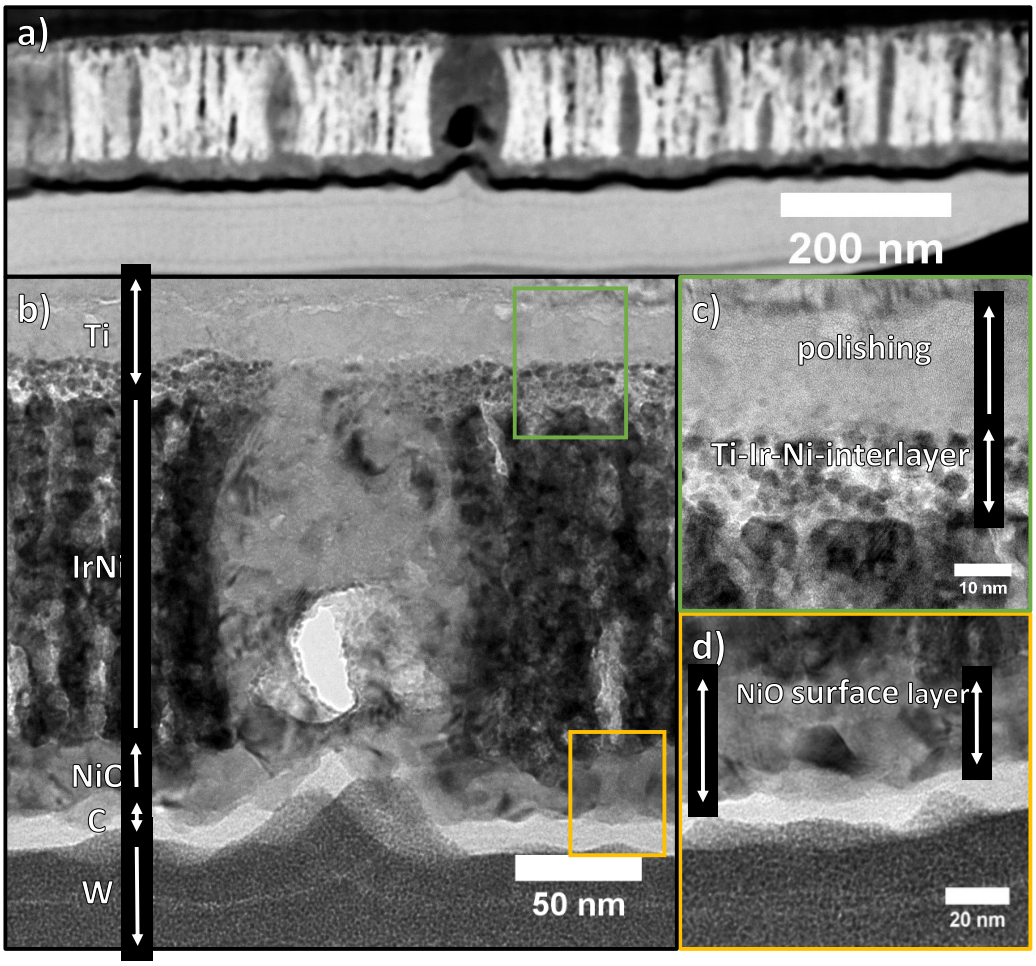

Fig. S7: TEM cross-section of IrNi/NiO HT-OER with a) an STEM ADF overview of the layer structure including pores and holes in the catalyst film and b) an additional overview with labeled components. Magnifications of c) the Ti-Ir-Ni interlayer between catalyst film and substrate as well as d) the NiO layer on the catalyst surface with darker spots indicating possible presence of Ir crystallites in the surface layer.

Fig. S7 depicts an overview of the catalyst structures observed in TEM cross-section of *IrNi/NiO HT-OER*. In Fig. S7a the titanium support is visible at the top, followed by a thin interlayer between support and catalyst layer. Thin pores and larger holes that penetrate the total layer depth characterize the catalyst layer. The pores as well as most of the larger holes are filled with a lighter material that is distinct from the Ti support or IrNi layers. Below the catalyst layer a second, thinner layer with similar contrast as the pores and holes is detected. Finally, the two protective layers of carbon and tungsten sputtered before and during the FIB-SEM preparation process complete the layer structure.

The catalyst layer (labeled "IrNi" in Fig. S7b) is significantly thicker than the original thickness observed in *IrNi-ap* (134 ± 3 nm vs. 87 ± 5 nm from SEM cross-section, compare Fig. S13). The pores extend to a diameter of 11 ± 4 nm while the holes have an average diameter of 59 ± 22 nm. Fig. S7c depicts a magnified view of the catalyst-support interlayer. Directly at the interface, a particulate layer of 13 ± 2 nm thickness has formed that closely resembles the Ti-Ir-oxide layer observed by Reier *et al.* on IrOx thin films calcined at 550 °C.[3] On top of the particulate layer a second, brighter layer (19 ± 3 nm) is visible throughout the cross-section that exhibits finer grain, which could be an effect of the polishing procedure applied to the Ti substrates during the preparation process. A higher magnification of the surface layer is shown in Fig. S7d showing an average layer thickness of 24 ± 6 nm. We note that even after the harsh OER conditions, this suface layer fully covers the catalyst surface over the whole length of the investigated TEM-lamella.

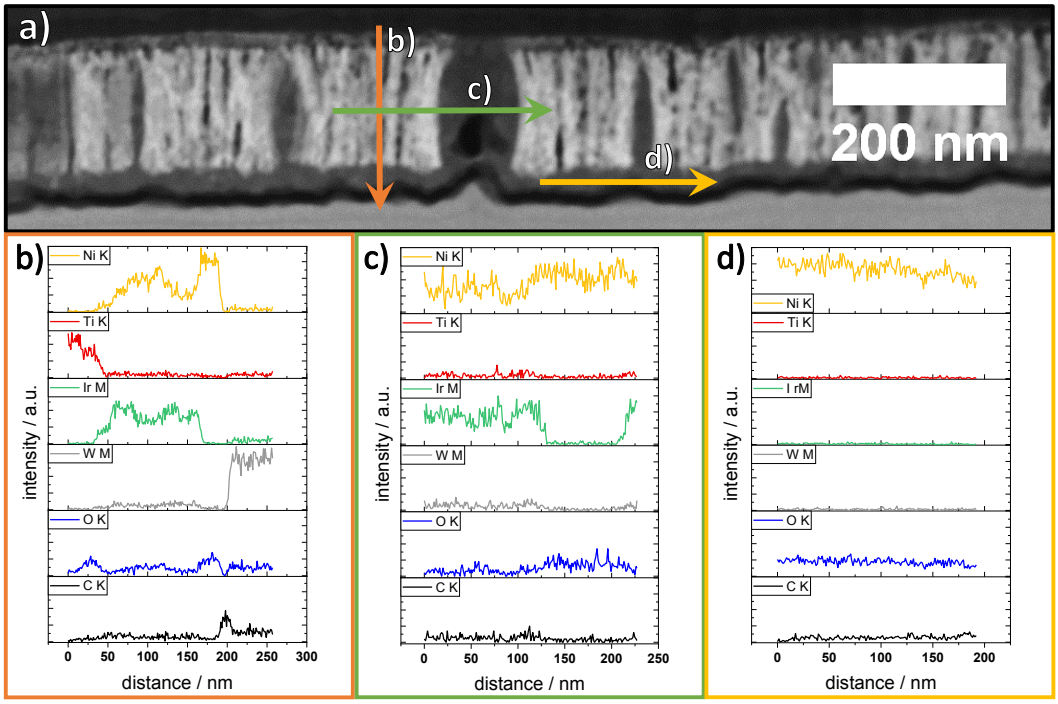

Fig. S8: The high-angle annular dark field (HAADF) image of the TEM cross-section of IrNi/NiO HT-OER in a) clearly shows the fiber-like remains of the IrNi layer and the surrounding channels, pores and holes that formed during the oxidation process. b), c) and d) STEM-EDX line scans along the directions indicated by colored arrows in a).

Fig. S8a shows a HAADF STEM image of a larger portion of the investigated *IrNi/NiO HT-OER* catalyst together with three STEM-EDX line scans through or along the catalyst layer. In Fig. S8a the fiber like structure of the remaining IrNi layer is clearly visible by the bright contrast of the IrNi alloy vs. the lower contrast of the catalyst surface as well as the pores and holes. The mixed brightness of the catalyst-support interlayer indeed indicates the presence of Ir and/or Ni in the Ti surface. The first EDX line scan (Fig. S8b) cuts through the catalyst layer structure from bottom (Ti support, top of Fig. S8a) to top (catalyst surface, bottom of Fig. S8a). Here, the Ti-Ir-Ni-mixed oxide layer at the catalyst-substrate interface becomes visible by the slow decrease of Ti and concurrent increase of Ir and Ni. The catalyst layer itself is clearly a mixture of Ir and Ni with slightly fluctuating intensities. Furthermore, the interface between IrNi and NiO surface layer is distinctly characterized by a sudden drop in Ir intensity concomitant with an increase in Ni and O intensity. The end of the line scan is dominated by signals from the C and W layers. A line scan along the porous IrNi layer is shown in Fig. S8c. The IrNi layer is characterized by varying intensities of Ir, Ni and little O, corresponding well to the pore/fibre structure observed in the HAADF. Here, the NiO filling inside the pores and holes is clearly visible. The composition of NiO is confirmed by line scan d) which shows counts for Ni, O and C from the contacting carbon layer only. In fact, intensities of Ti and Ir are below the detection limit. Note, however, that the general low intensity during the line scan can be an issue for detecting very low amounts of Ir inside the NiO layer. The observation of holes and pores in the bulk IrNi and the NiO overlayer indicated a distinct oxidation process of IrNi in the presence of low partial pressures of oxygen.

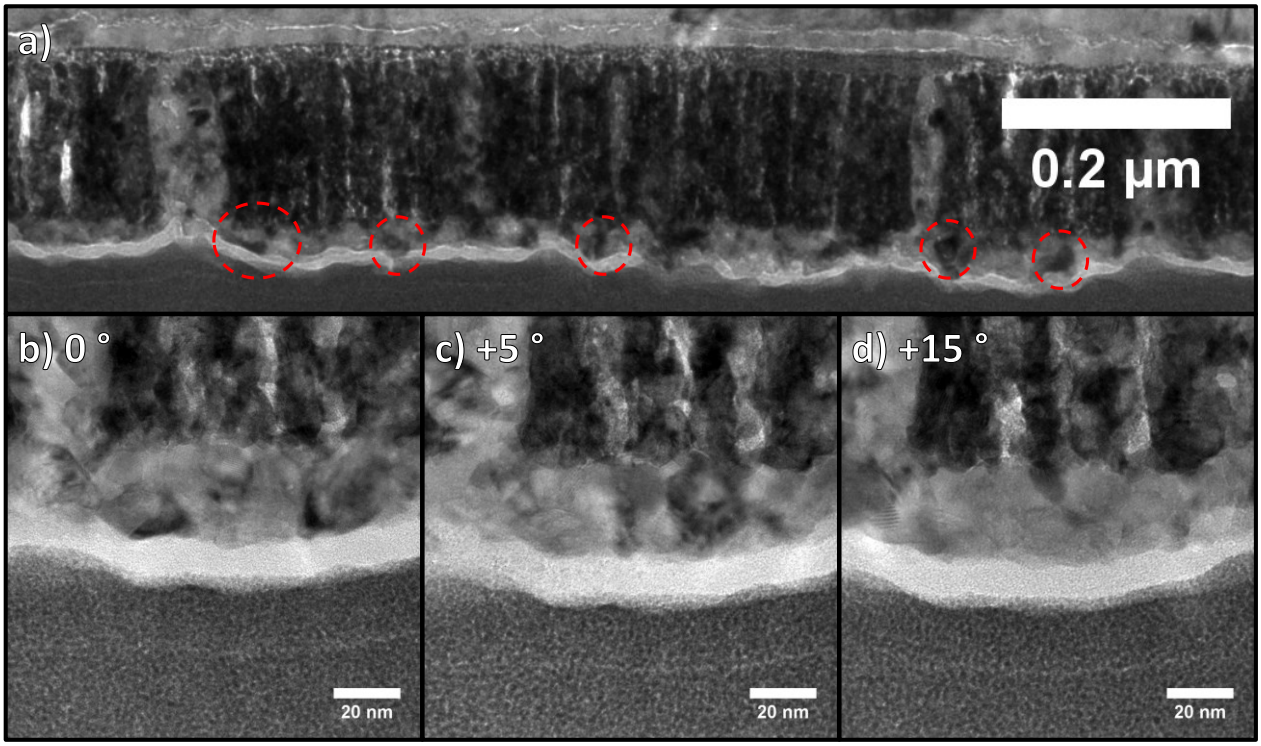

Fig. S9: TEM overview image a) of darker crystallites in the surface layer and TEM images of the same spot with b) 0 °, c) 5 ° and d) 15 ° tilting angle showing that darker contrast in the NiO layer crystallites can be an orientation effect.

In Fig. S9a multiple crystallites are visible in the surface layer that fit well to the Rietveld-determined crystallite size of 11 ± 2 nm of NiO. Some of the observed crystallites exhibit a darker contrast indicating possible inclusion of Ir. However, tilting the image as shown in Fig. S9c-d reveals most of them to be orientation effects of superimposed particles.

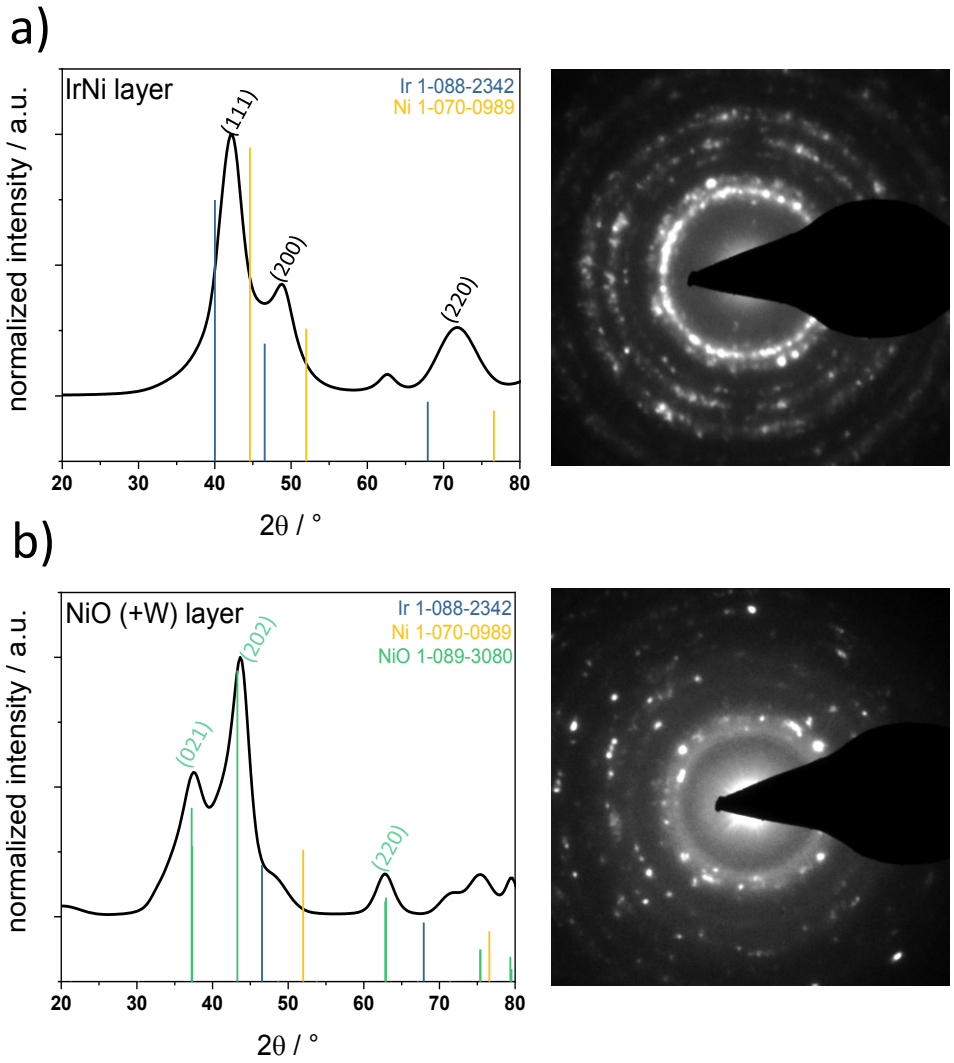

Fig. S10: SAED-derived diffraction patterns of a) the IrNi catalyst layer and b) the NiO surface layer (shown in Fig. S7c) alongside with the SAED images. The major reflexes of the identified structures are labeled with the corresponding crystal lattices. The SAED patterns were converted to diffraction patterns at Cu K-α scale with the PASAD plugin package (Gatan Digital Micrograph). PDF files of Ir, Ni and NiO are depicted by colored lines and indexed in the top right corner of each plot.

In order to elucidate the physicochemical background of the OER activity of *IrNi/NiO HT*, TEM-SAED was employed on the IrNi bulk as well as the NiO layer. Fig. S10a) depicts the corresponding pattern to the IrNi bulk layer that is well in line with the XRD pattern shown in Fig. S2. The unindexed reflex at ~63 °2θ fits

well to the NiO diffraction pattern shown in Fig. S10b, which is another indication for the NiO filling of pores and holes observed in the IrNi layer. The diffraction pattern in Fig. S10b finally identifies the surface layer as NiO by comparison to the corresponding PDF. Despite the absence of Ir in the corresponding linescan in Fig. S8d the diffraction pattern exhibits two shoulders at ~49 °2θ and ~72 °2θ that fit well to a small contribution of IrNi. This could be a first indication of Ir being present in the surface layer but may as well stem from excitation of the IrNi layer close to the IrNi-NiO interface.

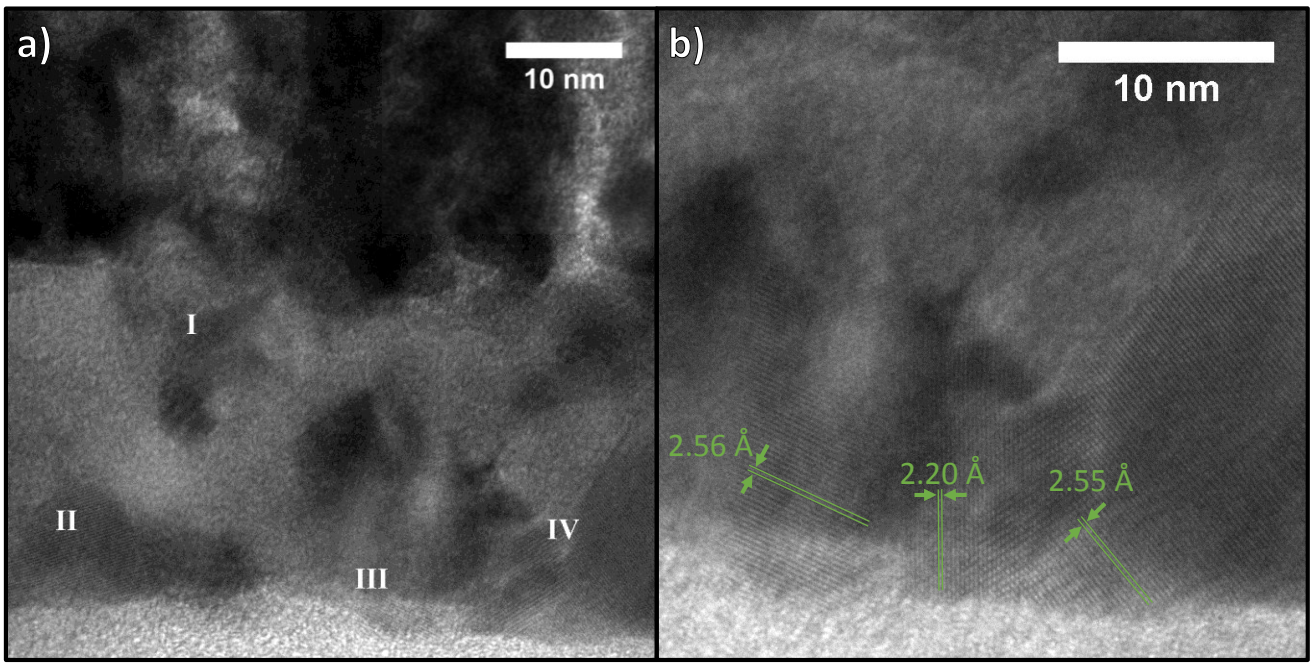

Fig. S11: High magnification TEM image of the surface layer in a) which shows lattice fringes being visible in regions I-IV. b) Magnification of regions III and IV with indicated lattice fringes.

Further indicators for Ir being present in the surface are depicted in Fig. S11a and b. Fig. S11a exemplarily shows an image with visible lattice fringes on crystallites in the NiO layer. Fig. S11b shows regions III and IV of Fig. S11a in higher magnification. The spacing of the observed lattice fringes was analyzed and assigned to corresponding d-values for this and multiple other images. Most regions in the analyzed images fit d-values of NiO lattices, thus, further validating the finding of a thick NiO surface layer on *IrNi/NiO HT*. The most prominent d-values (2.09 Å and 2.43 Å) correspond well to d-values of NiO: d(2 0 2) = 2.089 Å and d(0 2 1) = 2.413 Å. However, there are regions, such as III and IV in Fig. S11, where the obtained d-values differ. Region *III* exhibits lattice fringes with a d-spacing of 2.23 Å, 2.56 Å and 3.13 Å. These values all fit to IrO_2 lattices of d(2 0 0) = 2.253 Å, d(1 0 1) = 2.586 Å and d(1 1 0) = 3.186 Å. Similarly, region *IV* is characterized by d-values of 2.20 Å, 2.55 Å and 3.18 Å. The deviation from the literature d-values may result from the formation of a mixed IrNi oxide in these crystallites as well as from the small domain size.
In agreement with the surface sensitive detection of Ir in *IrNi/NiO HT-OER* by XPS, regions such as *III* and *IV* could indicate the presence of mixed IrNi (oxide) crystallites in the surface layer.

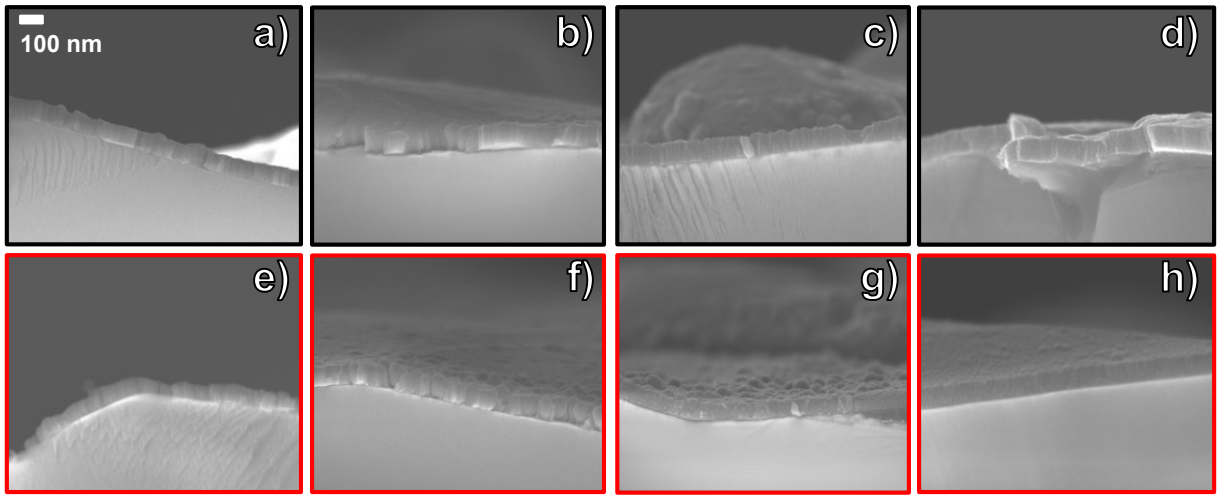

Fig. S12: SEM cross-section examples of the -ap samples. a) Ir, b) IrNi, c) IrOx, d) IrNiOx, e) Ir HT, f) IrNi HT, g) IrOx HT and h) IrNiOx HT. Scale bar in a) is valid for all subfigures.

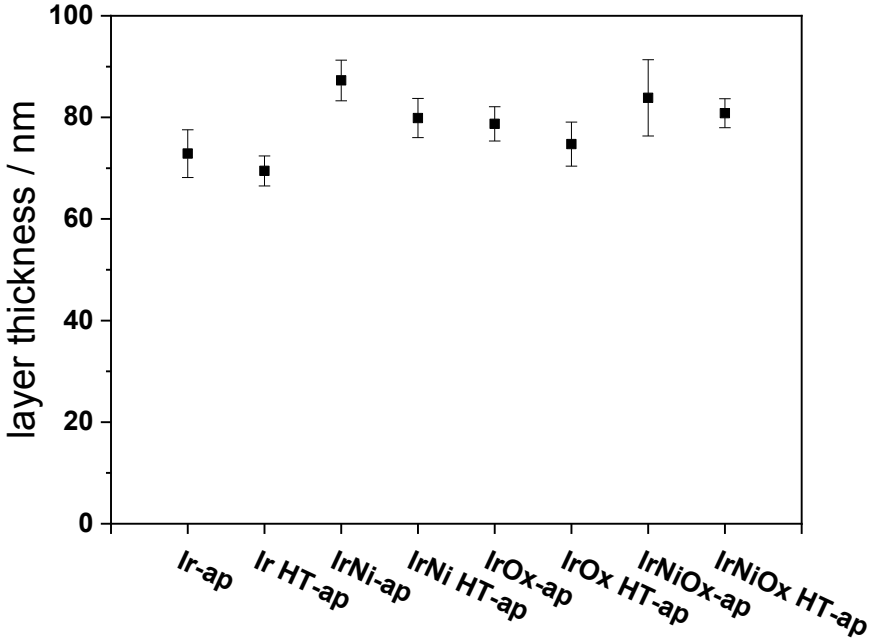

Fig. S13: Layer thickness obtained by SEM cross-section on the -ap samples.

SEM cross-section of the –*ap* samples (Fig. S12) reveals a layer thickness of ~ 80 nm on average (*Fig. S13*). Heat treatment leads to minimal shrinking of the layer thickness, probably due to sintering of the layers.

Bulk and surface oxygen content

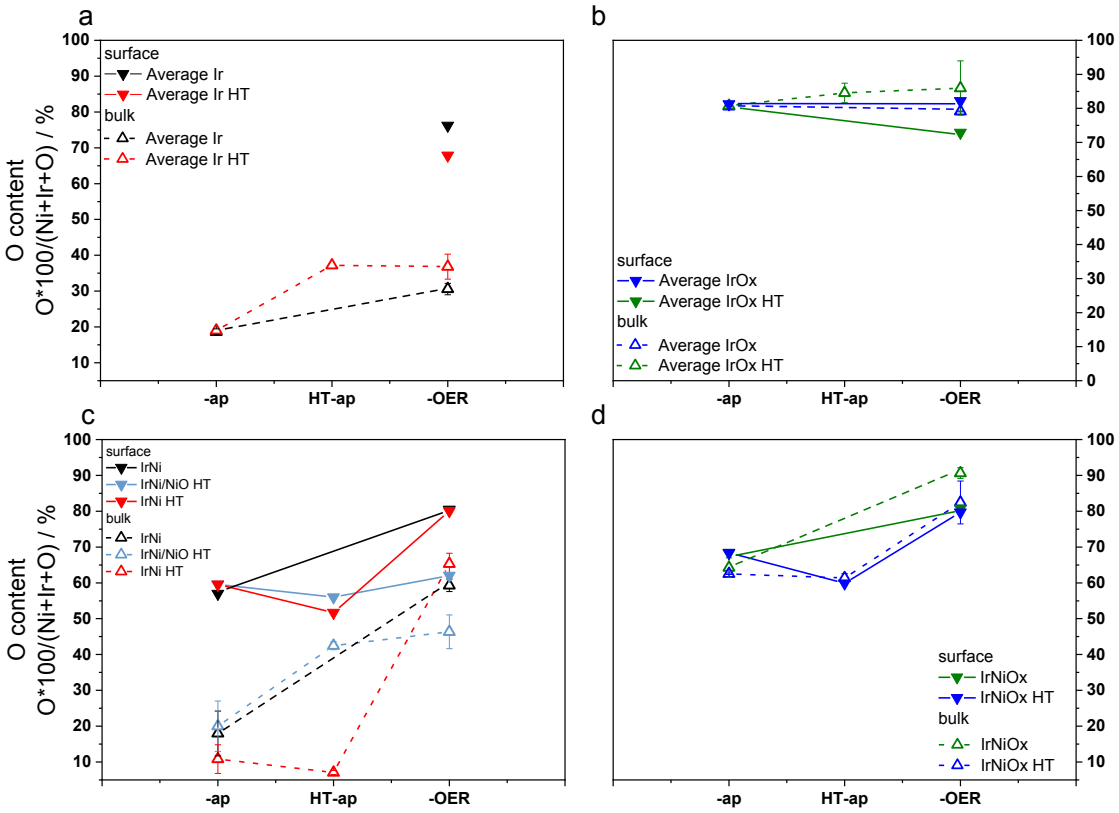

Fig. S14: Bulk (SEM-EDX) and surface (XPS) oxygen content of a) *Ir* and *Ir HT*, b) *IrOx* and *IrOx HT*, c) *IrNi(/NiO) (HT)* samples as well as d) *IrNiOx (HT)* samples. Contents were calculated as given on the corresponding y-axes. Note: for the XPS data Ti-Ox contributions on *IrOx-OER* and *IrNi HT-OER* were subtracted before calculating the O content (see experimental). For EDX data Ti was not included in the calculation.

The O content shown in Fig. S14 should not be understood as real oxygen content of the catalytic layer because of detection of underlying Ti oxides (mostly EDX) and possible organic species on the surface (EDX and XPS). However, it does give an indication about the change within the catalysts during electrocatalysis.

XPS data

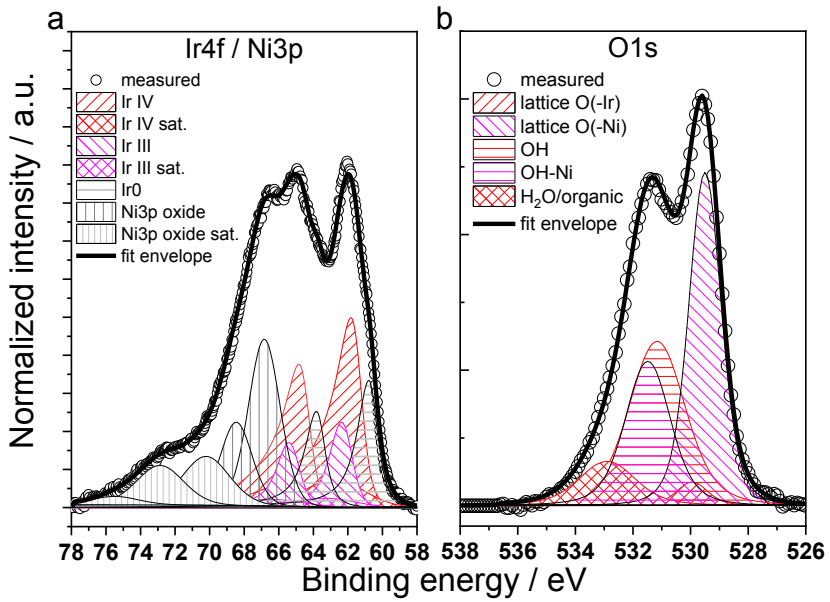

Fig. S15: a) Ir4f/Ni3p and b) O1s spectra and fits of IrNi/NiO HT-OER

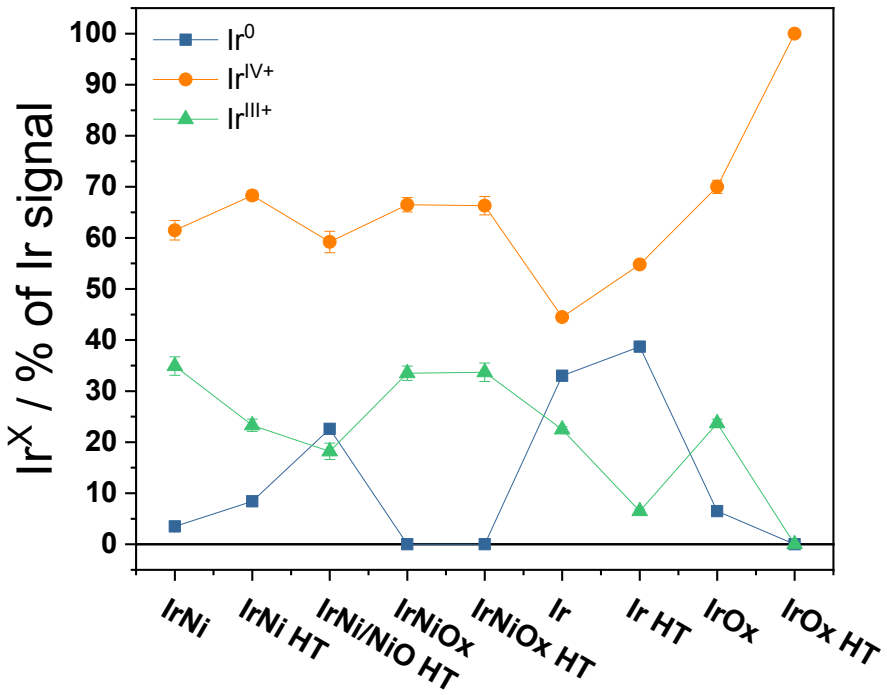

Fig. S16: Ir species detected in the Ir4f spectra of the -OER samples.

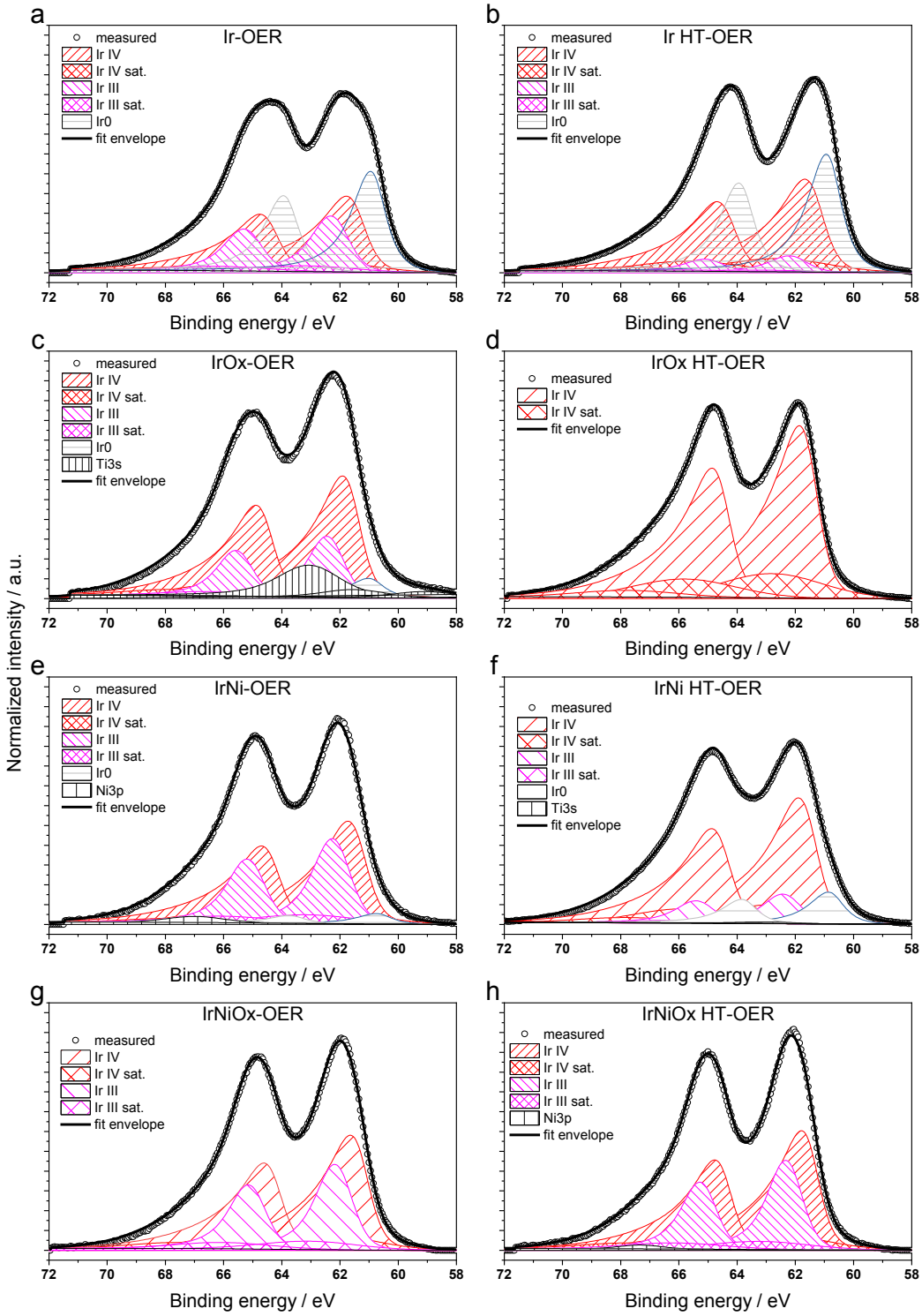

Fig. S17: Ir4f spectra of the –OER samples with their corresponding fits.

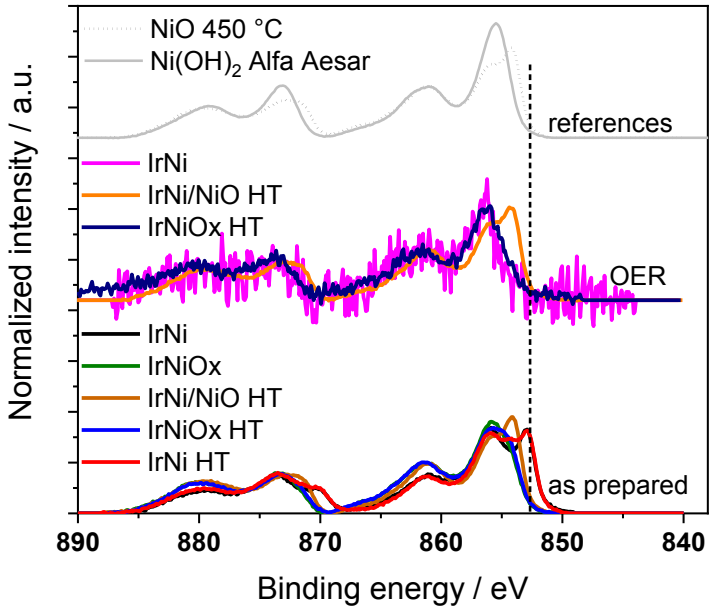

Fig. S18: XPS spectra of the Ni2p region in the -ap and -OER states of Ni containing samples as well as reference spectra for NiO and $Ni(OH)_2$. The position of metallic Ni2p(3/2) is given by the vertical dashed line.

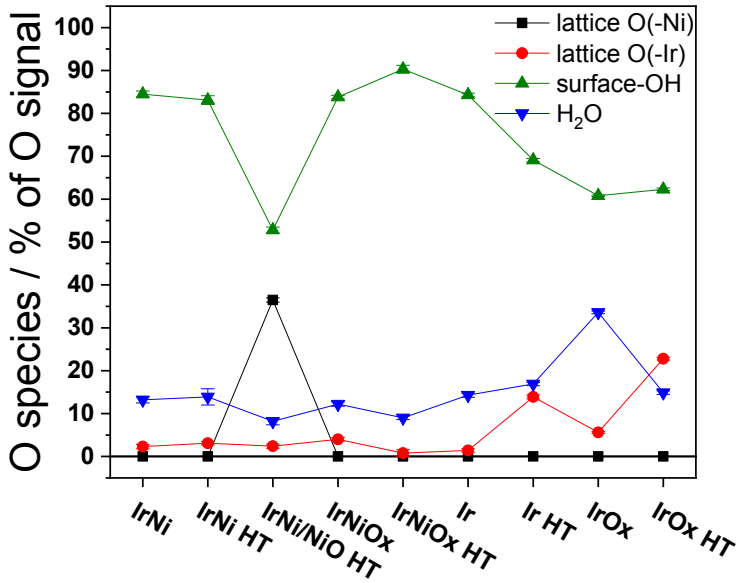

Fig. S19: O species detected in the O1s signal of the -OER samples. TiOx contributions were below 0.3 % for all samples except IrOx-OER (plus a minor TiOx contribution on IrNi HT-OER) and thus neglected in the calculations. On IrOx-OER and IrNi HT-OER TiOx contributions were included in the fit by fixing the positions to reference measurement of TiOx-OER (see experimental part in the main manuscript). The obtained Ti contributions were then excluded in the calculation of the OH surface concentration.

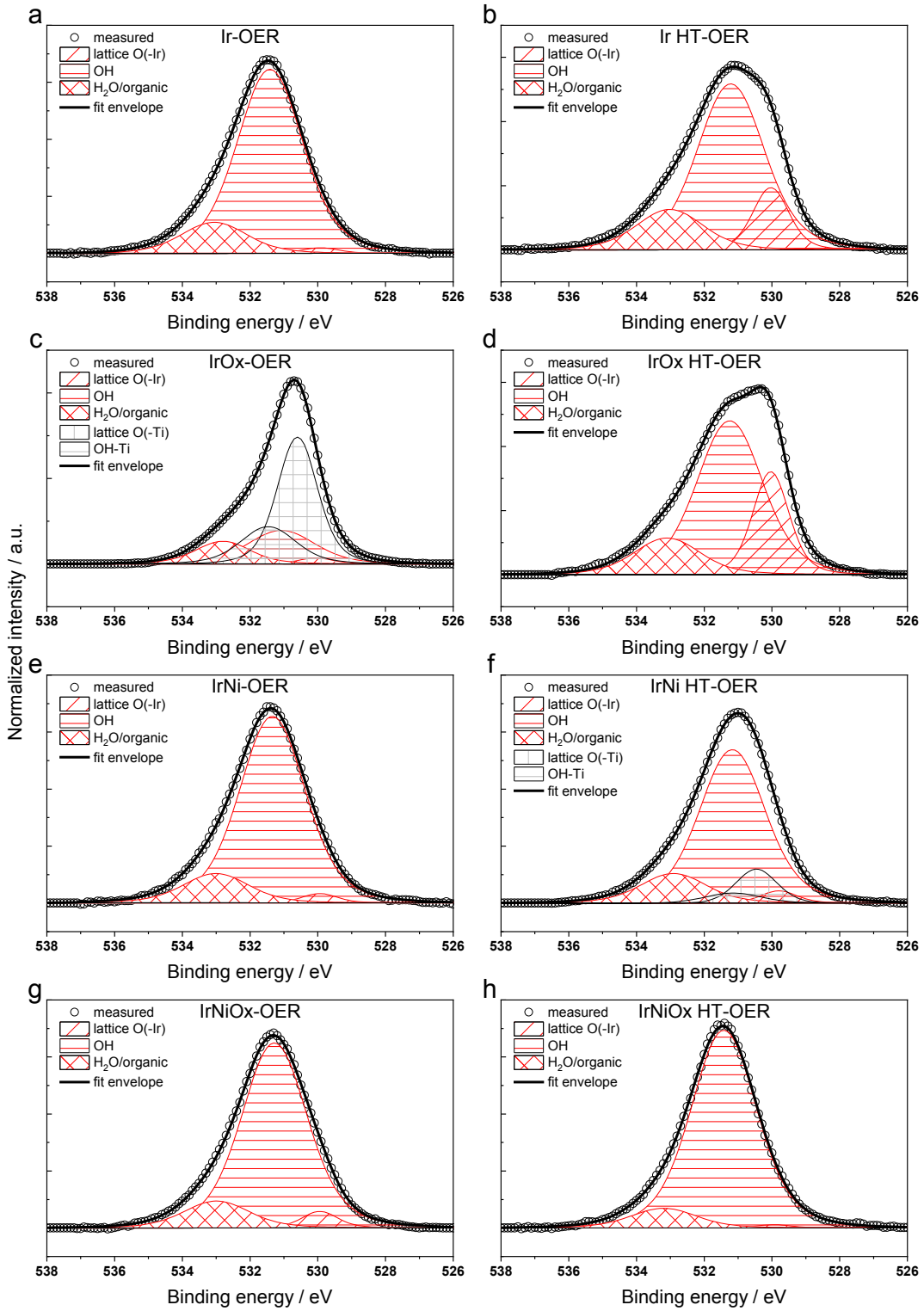

Fig. S20: Fitted O1s spectra of the -OER state of the investigated sample set.

Oxide formation on IrNi bimetallic alloys

As shown by STEM cross-section analysis, the IrNi bulk layer of *IrNi/NiO HT-OER* was characterized by pores and holes filled with NiO. STEM-EDX line scans (see Fig. S8) revealed a clear distinction between the IrNi bulk and NiO surface layers, whereas indications for Ir-containing crystallites were found inside the NiO layer by analysis of lattice fringes. Unutulmazsoy *et al*. recently reported the formation of a NiO surface layer during heat treatment of Ni and Ni alloys at low partial pressures of oxygen in the range of 250-500 °C.[5] During oxidation, enhanced Ni diffusion along the grain boundaries of NiO seeds leads to the observed pore/hole formation as well as segregation of Ni based alloys in their study, which is in good agreement with the SEM and (S)TEM observations on *IrNi/NiO HT-OER*. Most likely, the catalyst layer expanded during the Ni oxidation due to the distinct diffusivities of Ir and Ni, especially in NiO as well as due to the NiO formation inside the formed pores and holes.
The highly corrosive conditions during OER led to Ni leaching on all samples even though the Ni content stayed high on *IrNi/NiO HT-OER* with the NiO bunsenite surface layer remaining mostly intact. Most likely, dissolution of Ni from the NiO surface during the OER subsequently exposed some of the observed pores to the electrolyte (see SEM and (S)TEM results; Fig. S5 and Fig. S7-11). However, most of the pores and holes were filled with NiO, thus, only minor parts of the subsurface IrNi layer should have got in contact with the electrolyte through open pores. Additionally, (S)TEM and SAED (see Fig. S9-11) indicated a low amount of Ir or IrNi crystallites within the NiO layer. Thus it appears that thinning of the NiO layer during OER could have left these crystallites exposed and oxidized once in contact with the electrolyte. Electrochemical oxidation of such crystallites should result in a similar IrNi-core/IrOx-shell crystallite structure as reported for *IrNi NPs* by Nong et al.[6] The latter is in line with the emerging Ir4f states. Given the IMFP of Ir4f and post-OER NiO layer thickness, ~23 % Ir^0 could not be attributed to the bulk IrNi layer underneath the NiO surface. Contrary, a metallic iridium contribution appeared only possible for a superficially oxidized Ir(Ni) shell of a metallic IrNi crystallite encapsulated in the NiO surface. Oxidized IrNi at the electrolyte interface inside the pores would have a similar effect. The high intrinsic activity of such IrNi NP-like structures distributed in the NiO surface (which showed an almost neglectable OER activity in acid) would therefore be a reasonable explanation of the observed activity of *IrNi/NiO HT*.

Of the other two bimetallic catalysts, *IrNi-OER* retained more Ni (surface: 6.4 at%, bulk: ~50 at% Ni) than *IrNi HT-OER* (surface: 0 at%, bulk: ~30 at% Ni). In combination with the emerging Ir-O lattice oxygen contribution and a remaining metallic Ir^0 component in XPS two resulting surface structures appeared possible. One can assume the formation of i) a mixed IrNiOx layer on the surface (similar to *IrNiOx TF*[4]), or ii) of a monometallic IrOx surface layer on top of a bimetallic IrNi bulk layer (multi-layer near-surface-alloy similar to IrNi@IrOx NPs[6]). Due to the fixed analysis depth of the lab-XPS data, both structures could not be distinguished for *IrNi-OER* in the present study. However, since the Ni2p spectrum of *IrNi-OER* was clearly resembling Ni^{II+} hydroxide, a mixed metal oxide surface layer seemed to be the most likely structure. Contrary, on *IrNi HT-OER* structure ii) similar to *IrNi NPs*[6] appeared to be the most plausible explanation

with no Ni detected by XPS. The formation of a rather thin (mixed metal) surface oxide layer on *IrNi-OER* and *IrNi HT-OER* was further supported by the remaining metallic contribution in the Ir4f peak as well as the IrNi metallic phase in the XRD. Taking recent findings on electrochemical surface oxidation of Ir into account[7] and comparing the minimal Ir^0 contributions on *IrNi-OER* to those on *IrNi HT-OER*, the formation of a thicker oxide layer on *IrNi-OER* seems quite plausible. The possible surface layer formation mechanisms on *IrNi(/NiO) (HT)* are presented in Fig. S21.

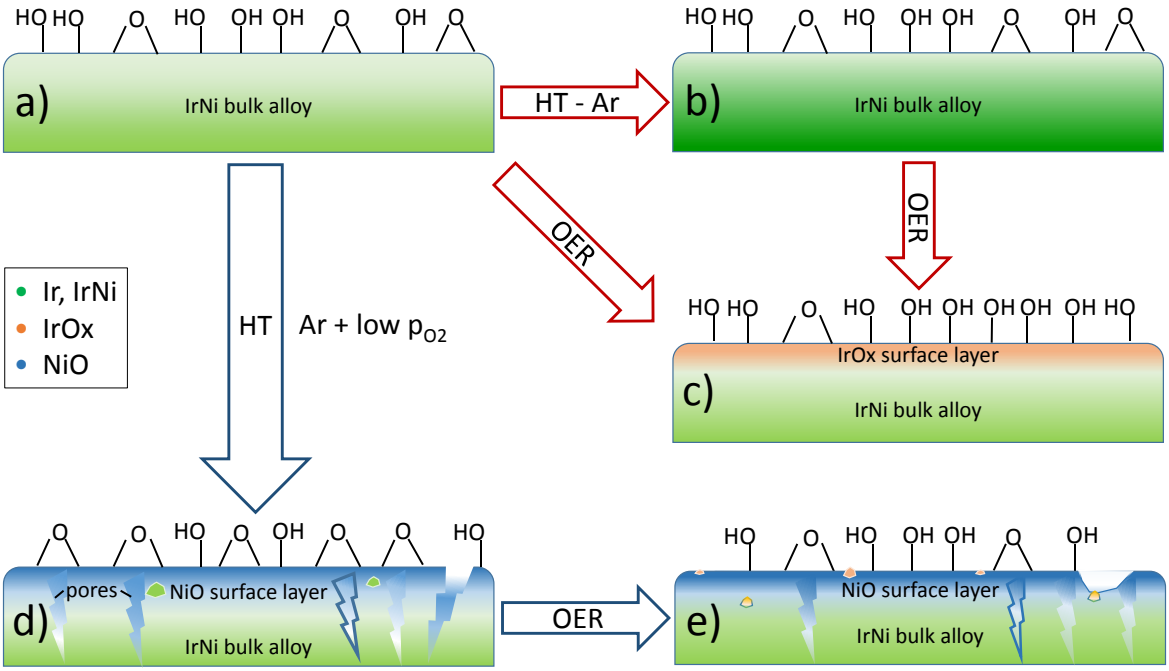

Fig. S21: Scheme of Ni leaching and surface oxide layer formation in *IrNi(/NiO) (HT)* samples. Starting from a) heat treatment in pure argon leads to b) an increased crystallinity but otherwise similar structures. Electrochemical leaching and oxidation of the metallic IrNi alloy [coming from a) or b)] leads to c) the formation of a Ni depleted IrOx surface layer with Ni being leached out completely on *IrNi HT-OER*. Heat treatment with traces of oxygen, however, results in d) surface oxidation, Ni segregation and the formation of pores in between the remaining metal and the NiO surface layer. The pores are (mostly) filled with NiO. Possibly, some Ir or IrNi particles remain in the NiO surface layer during thermal oxidation. Upon electrochemical oxidation and leaching of d) the NiO layer is thinning, allowing, as shown in e), electrolyte to come into contact with IrNi crystallites in the NiO layer or through open pores to the underlying IrNi layer. IrNi in contact with electrolyte is immediately oxidized and forms the active species of *IrNi/NiO HT-OER*.

In comparison to the metallic catalysts, the bimetallic oxides exhibited similar structures. *IrNiOx-OER* lost all its surface Ni while *IrNiOx HT-OER* retained about 20.6 at% Ni in the surface layer. In this, both catalysts were resembling the template *IrNiOx TF* catalysts[4]. We conclude that the oxide structure on *IrNiOx HT-OER* must have been similar to that on *IrNiOx TF* with a lower starting composition of 67 at% Ni, whereas that of *IrNiOx-OER* fit well to the structure observed on *IrNiOx TF* with 80 at% Ni starting composition. This indicates the improved stability and Ni retention in the heat-treated mixed oxide. Despite their quite distinct nominal Ni content, the surface layers on *IrNi-OER* and *IrNiOx HT-OER* appeared very similar and are likely

a key reason for their similar, outstanding specific OER activities. The additional performance boost on *IrNi HT-OER* might stem from the formation of a pure IrOx surface layer on top of a metallic bulk layer and as such a “core-shell”-like structure with distinct intrinsic activity as observed in *IrNi NPs*.[6]

Additional geometric electrochemical activities

Table S2: Steady state geometric current densities at the three most commonly used potentials vs. RHE for the investigated sample set as well as the reference catalysts. Data in grey was obtained using Origin's "digitizer" function and should be treated with higher uncertainty. Data in bold: This study.

sample	j_{geo} / mA cm^{-2}		
	1.50 V	1.53 V	1.55 V
Ir	**1.5**	**6.4**	**13.1**
Ir HT	**0.3**	**0.8**	**1.6**
IrNi	**5.0**	**16.8**	**25.9**
IrNi HT	**7.3**	**24.2**	**36.7**
IrNi/NiO HT	**0.5**	**1.6**	**3.6**
IrOx	**0.3**	**0.7**	**1.3**
IrOx HT	**0.3**	**1.4**	**3.6**
IrNiOx	**0.8**	**2.6**	**5.0**
IrNiOx HT	**3.2**	**9.9**	**24.5**
IrNiOx TF	1.4	5.7	11.7
IrNi NPs	0.7	3.2	7.2
Elyst Ir75	**0.1**	**0.3**	**0.75**

Supporting Experimental Procedures

Sample preparation

Ir(Ni)(O) coatings were deposited by reactive DC magnetron sputtering using Ir and Ni metallic targets on a rotating substrate holder in the presence of argon–oxygen reactive gas mixtures at UTBM. Besides polished Ti cylinders, glass slides, alumina and Si wafers were used as substrates. The received samples were investigated as prepared or subjected to an additional heat treatment at TU Berlin. The experimental device was a 90 L sputtering chamber (Alcatel 604) pumped down via a turbo-molecular pump, allowing a base vacuum of about 10^{-4} Pa.[8] The argon and oxygen flow rates introduced in the deposition chamber were controlled with Brooks flowmeters and the total pressure was measured using a MKS Baratron Gauge. The films were deposited at a total pressure of about 4.5 Pa. The Ir target (50 mm in diameter and 1 mm thick) and the Ni target (50 mm in diameter and 3 mm thick) were mounted on a balanced magnetron cathode with a target-to-substrate working distance of 100 mm. The Ir target was powered by pulsed DC supply (Advanced Energy Pinnacle+) with a discharge current of 0.25 A pulsed at 70 kHz and the discharge current applied on Ni target was adjusted to obtain a convenient composition. The main sputtering parameters are summarized in Table S3.

Table S3: Sputtering parameters

Ar flow rate / sccm	200	Discharge current - Ir / A (kHz)	0.25 (70)
O2 flow rate / sccm	20	Discharge current - Ni / A (kHz)	0 to 0.63 (75)
Total pressure / Pa	4.2 to 4.4	Around sputtering time / min	3 to 17

Samples were heat treated at TUB in a rapid temperature tube furnace with a moving heating stage (MTI Corp., USA). The heating stage was preheated to 450 °C and then slid over the sample with the latter being at room temperature. In order to compensate for the unavoidable cooldown the heat treatment was applied for 20 min, resulting in 15 min at 450 °C as in the *IrNiOx TF* synthesis.[4] Afterwards, the heating stage was slid back to achieve rapid cooling of the samples. For the metallic samples the tube furnace was purged with Ar (4.6, Air Liquide) for 24 h before starting and during the heat treatment. The heat treatment of *IrNi/NiO HT* was identical to the metallic samples but after a shorter Ar purging period of 2 h. The oxidic samples were heat treated in synthetic air (20 % O_2 in 80 % N_2, Air Liquide).

Physicochemical characterization

Mass loading was calculated by the initial layer thickness obtained by SEM cross-section and the material density. For SEM cross-section the samples supported on Si and alumina wafers were broken in half and immediately introduced into the SEM sample chamber to observe the cross-section.

A (S)TEM cross-section of *IrNi/NiO HT-OER* was acquired by preparing a TEM lamella by Focussed Ion Beam (FIB). A FEI Helios NanoLab 600 workstation equipped with an Omniprobe lift-out system, a Pt & W gas injector system, and a scanning electron microscope (SEM) detector was used. Prior to the FIB preparation the film was coated with carbon using a Leica EM ACE600, the resulting carbon layer worked as a spacer between the IrNi film and the sputtered W. The TEM and STEM measurements were performed at a FEI Tecnai $G^2$20 S-TWIN transmission electron microscope with a LaB_6 cathode operated at an accelerating voltage of 200 kV. TEM images were collected with a CCD camera (GATAN MS794 P). Furthermore, the microscope is equipped with a DISS5 Scanning Unit (point electronic GmbH) and a BF/ADF/HAADF Detector "STEM-22-4-3-BF15" (PN Detectors) to provide STEM mode. The STEM images itself were collected using the software SEM Control Version 5.15.8.0 (point electronic GmbH) and processed with Digital Image Processing System (DIPS) Version 2.9.4.0 (point electronic GmbH). EDX measurements, including the line scans in STEM mode, were performed with the software Genesis Spectrum (Version 6.53, EDAX Inc). The SAED evaluation was performed with the PASAD[9-10] plugin in Gatan Digital Micrograph™. The obtained reciprocal distances were transferred to Cu K-α scale to compare the calculated diffraction patterns to the PDF database. All electron micrographs (SEM, TEM and STEM) were evaluated with ImageJ (Version 1.48, W.S. Rasband, NIH, USA).

XPS fitting and data evaluation

Only on *IrOx-OER* a significant amount of TiOx was detected due to the severe delamination. On *IrNi HT-OER* a small TiOx (~0.6 % Ti) contribution was detected as well. The Ti-O contributions to the O1s spectra were fitted in analogy to an uncoated Ti disc that underwent the same electrochemical protocol (*TiOx-OER*) and subsequently excluded when calculating the OH concentration. This is plausible as TiOx does not show any OER-activity in the investigated potential range.[11] All other samples show TiOx contributions below 0.3 % and thus, Ti-O contributions in the O1s spectra were neglected on those samples.

The Ir^{III+}-surface concentration depicts the amount of reduced iridium in the surface. The Ir^{III+}-surface concentration was calculated by dividing the Ir^{III+} contribution of the Ir4f spectra by the sum of Ir^{III+} and Ir^{IV+} contributions as Ir^0 was considered to not participate in the reaction. The OH-surface concentration was calculated by dividing the OH contribution of the O1s spectra by the sum of OH contribution and Ir-O lattice oxygen contribution. For the OH-surface concentration in this study, Ni-O lattice oxygen is not considered since none of the catalysts except *IrNi/NiO HT-OER* show any Ni-O lattice contribution in their –*OER* state. In *IrNi/NiO HT-OER*, the Ni-O lattice is a separate phase according to XRD and thus can be considered as not contributing to the acidic OER activity in the investigated potential range.[4] In catalysts such as *IrNiOx TF* where a mixed metal oxide surface layer has been convincingly proven Ni-O lattice oxygen should be included in this measure. Owing to the high degree of delamination on *IrOx-OER* a high fraction of Ti-O and Ti-OH could be detected, which was also excluded from the calculation of the OH-surface concentration as Ti oxides are considered non-contributing to the OER in the investigated potential range.[11]

Electrochemical protocol

In short, electrodes were immersed in degassed electrolyte (15 min, N_2) at 1.0 V_{RHE} followed by three scans in the OER region. The first and third scan are slow CVs (6 mV s^{-1}) into the OER region, starting from 1.0 V up to a current density of 15 mA cm^{-2}. The second scan was performed as stepped potential voltammetry (SPV). Starting at a potential corresponding to 0.01 mA cm^{-2} the potential is stepped up by 20 mV until a current density of 15 mA cm^{-2} is reached. At every step, the current is recorded for 5 min to obtain the steady state activity. Subsequently electrochemical impedance spectroscopy (EIS) is measured at the same potential. For evaluation the last 20 s of each step are averaged. After the OER scans, the electrolyte was degassed again while holding the working electrode potential at 1.0 V. Subsequently, cyclic voltammetry (CV) between 0.4 and 1.4 V_{RHE} at various scan rates (500, 200, 100, 50, 20 and 10 mV s^{-1}, 100 cycles at 500 mV s^{-1} and 3 cycles at each following scan rate) was measured. Finally, the lower turning potential was extended to 0.05 V_{RHE} and the CVs were repeated. The whole protocol was repeated once for each sample to obtain steady state data of the catalysts. CVs and OER scans were conducted at 0 rpm and 1600 rpm, respectively. Ohmic drop correction was calculated with the high frequency resistance obtained from electrochemical impedance spectroscopy (EIS) at 1.0 V_{RHE} and at elevated OER-potentials. The total anodic charge Q_{anodic} of the samples was obtained from the third 0.4 – 1.4 V_{RHE} CV at 50 mV s^{-1}.

To calculate the specific current density, the recorded current I [mA] was divided by Q_{anodic} [mC]. This has been established as a relative measurement for the available electrochemical surface area on iridium based thin film catalysts.[3, 12] OER activities were extracted from the SPV OER scans. The SPV taken in the beginning of the test is denoted as initial activity whereas the data taken from the SPV in the repetition of the protocol is denoted as steady state activity.

Specific activity normalization

Albeit being the most comprehensive figure of merit for comparing application-oriented activities, mass activity might not necessarily be the best choice for mechanistic or structural investigations. Especially when comparing monometallic (oxide) catalysts with mixed or doped catalysts it is easy to miss activity descriptors because of the – in this case – biased figure of merit. The reference catalyst *Ir-OER* naturally showed a much lower mass activity but reached similar specific activities as *IrNiOx-OER* and, despite catalyst loss, the latter compares well to *IrNiOx HT-OER* (compare Fig. 1a in the main manuscript). The latter shows that specific activity obtained by normalizing to Q_{anodic} allows the exclusion of superimposed effects such as physical catalyst loss etc. Hence, however normalized, the figure of specific activity is making mechanistic comparison possible in the first place. We acknowledge that normalizing the current by Q_{anodic} is not ideal either as this method is limited to thin film or unsupported catalysts. On supported catalysts the capacitive component of the support will distort Q_{anodic} and alternatively the charge under the Ir^{III+}/Ir^{IV+} peak Q_{Ir} is often used.[2] Unfortunately, the latter is not always accessible on IrOx films (see Fig. 1b, c in the main manuscript). However, as Q_{anodic} will always be larger than Q_{Ir}, its use will only underestimate the activity, if at all. Additionally, as discussed above, normalization by Q_{anodic} has proven to be an excellent measure when comparing specific activities despite obvious catalyst loss. Thus, by lacking a better alternative, Q_{anodic} (being an accepted measure on thin films) was used here, too.

1. Supporting References

1. Hamalainen, J.; Hatanpaa, T.; Puukilainen, E.; Sajavaara, T.; Ritala, M.; Leskela, M., Iridium metal and iridium oxide thin films grown by atomic layer deposition at low temperatures. *J Mater Chem* **2011,** *21*, 16488-16493.
2. Nong, H. N.; Gan, L.; Willinger, E.; Teschner, D.; Strasser, P., IrOx core-shell nanocatalysts for cost- and energy-efficient electrochemical water splitting. *Chem Sci* **2014,** *5*, 2955-2963.
3. Reier, T.; Teschner, D.; Lunkenbein, T.; Bergmann, A.; Selve, S.; Kraehnert, R.; Schlogl, R.; Strasser, P., Electrocatalytic Oxygen Evolution on Iridium Oxide: Uncovering Catalyst-Substrate Interactions and Active Iridium Oxide Species. *J Electrochem Soc* **2014,** *161*, F876-F882.
4. Reier, T.; Pawolek, Z.; Cherevko, S.; Bruns, M.; Jones, T.; Teschner, D.; Selve, S.; Bergmann, A.; Nong, H. N.; Schlögl, R.; Mayrhofer, K. J. J.; Strasser, P., Molecular Insight in

Structure and Activity of Highly Efficient, Low-Ir Ir–Ni Oxide Catalysts for Electrochemical Water Splitting (OER). *J Am Chem Soc* **2015,** *137*, 13031-13040.
5. Unutulmazsoy, Y.; Merkle, R.; Fischer, D.; Mannhart, J.; Maier, J., The oxidation kinetics of thin nickel films between 250 and 500 °C. *Phys Chem Chem Phys* **2017,** *19*, 9045-9052.
6. Nong, H. N.; Oh, H. S.; Reier, T.; Willinger, E.; Willinger, M. G.; Petkov, V.; Teschner, D.; Strasser, P., Oxide-Supported IrNiOx Core-Shell Particles as Efficient, Cost-Effective, and Stable Catalysts for Electrochemical Water Splitting. *Angew Chem Int Edit* **2015,** *54*, 2975-2979.
7. Li, T.; Kasian, O.; Cherevko, S.; Zhang, S.; Geiger, S.; Scheu, C.; Felfer, P.; Raabe, D.; Gault, B.; Mayrhofer, K. J. J., Atomic-scale insights into surface species of electrocatalysts in three dimensions. *Nature Catalysis* **2018,** *1*, 300-305.
8. Pour Yazdi Mohammad, A.; Briois, P.; Lapostolle, F.; Billard, A., SrZr1-xYxO3 Coatings Elaborated by DC Magnetron Sputtering. *ECS Trans.* **2007,** *7*, 2313-2319.
9. PASAD. http://www.univie.ac.at/pasad/ (accessed access date: 18.05.18).
10. Gammer, C.; Mangler, C.; Rentenberger, C.; Karnthaler, H. P., Quantitative local profile analysis of nanomaterials by electron diffraction. *Scripta Materialia* **2010,** *63*, 312-315.
11. Johnson, B.; Girgsdies, F.; Weinberg, G.; Rosenthal, D.; Knop-Gericke, A.; Schlogl, R.; Reier, T.; Strasser, P., Suitability of Simplified (Ir,Ti)O-x Films for Characterization during Electrocatalytic Oxygen Evolution Reaction. *J Phys Chem C* **2013,** *117*, 25443-25450.
12. Spöri, C.; Kwan, J. T. H.; Bonakdarpour, A.; Wilkinson, D. P.; Strasser, P., The Stability Challenges of Oxygen Evolving Catalysts: Towards a Common Fundamental Understanding and Mitigation of Catalyst Degradation. *Angew Chem Int Ed* **2017,** *56*, 5994-6021.